JTTEE5 19:198–206
DOI: 10.1007/s11666-009-9429-8
1059-9630/$19.00 © ASM International

Porous Architecture of SPS Thick YSZ Coatings Structured at the Nanometer Scale (~50 nm)

Antoine Bacciochini, Ghislain Montavon, Jan Ilavsky, Alain Denoirjean, and Pierre Fauchais

(Submitted April 23, 2009; in revised form August 28, 2009)

Suspension plasma spraying (SPS) is a fairly recent technology that is able to process sub-micrometer-sized or nanometer-sized feedstock particles and permits the deposition of coatings thinner (from 20 to 100 μm) than those resulting from conventional atmospheric plasma spraying (APS). SPS consists of mechanically injecting within the plasma flow a liquid suspension of particles of average diameter varying between 0.02 and 1 μm. Due to the large volume fraction of the internal interfaces and reduced size of stacking defects, thick nanometer- or sub-micrometer-sized coatings exhibit better properties than conventional micrometer-sized ones (e.g., higher coefficients of thermal expansion, lower thermal diffusivity, higher hardness and toughness, better wear resistance, among other coating characteristics and functional properties). They could hence offer pertinent solutions to numerous emerging applications, particularly for energy production, energy saving, etc. Coatings structured at the nanometer scale exhibit nanometer-sized voids. Depending upon the selection of operating parameters, among which plasma power parameters (operating mode, enthalpy, spray distance, etc.), suspension properties (particle size distribution, powder mass percentage, viscosity, etc.), and substrate characteristics (topology, temperature, etc.), different coating architectures can be manufactured, from dense to porous layers, from connected to non-connected network. Nevertheless, the discrimination of porosity in different classes of criteria such as size, shape, orientation, specific surface area, etc., is essential to describe the coating architecture. Moreover, the primary steps of the coating manufacturing process affect significantly the coating porous architecture. These steps need to be further understood. Different types of imaging experiments were performed to understand, describe and quantify the pore level of thick finely structured ceramics coatings.

Keywords coating architecture, porosity quantification, suspension plasma spraying, ultra-small-angle x-ray scattering

1. Introduction

Optimization of finely structured ceramic coatings manufactured by suspension plasma spraying (SPS) of nano- or sub-micrometer-sized feedstock is the objective of intensive researches around the world. Promising results have been obtained when considering such coatings either for thermal insulation (thermal barrier coatings (TBCs)) or functional ceramic layers as those required in solid oxide fuel cell (SOFC) systems (Ref 1-4). From a general point of view, TBCs apparent thermal conductivity and behavior under thermomechanical loads depend, besides the coating composition, upon its porous architecture, whereas SOFC electrolyte must be as dense as possible without any connected pores and low stacking defect density.

Pawlowski and Fauchais (Ref 5) identified four classes of stacking defects in plasma sprayed coatings. In the case of micrometer-sized ceramic coatings manufacturing by atmospheric plasma spraying (APS), the coating is characterized by (i) its anisotropic lamellar structure; (ii) its void (or globular pore content) which results from stacking defects between lamellae; (iii) intralamellar cracks resulting from stress relaxation during lamella rapid solidification (i.e., average cooling rate of the order of 10^6 $K \cdot s^{-1}$) after spreading; (iv) interlamellar delaminations due to poor contact between flattened lamellae. The combination of these features generates a complex 3-D interconnected network of pores (Ref 6).

SPS is a recent technology and an alternative to conventional APS to manufacture thinner coatings due to the specific size of the feedstock particles, from a few tens of

This article is an invited paper selected from presentations at the 2009 International Thermal Spray Conference and has been expanded from the original presentation. It is simultaneously published in *Expanding Thermal Spray Performance to New Markets and Applications: Proceedings of the 2009 International Thermal Spray Conference*, Las Vegas, Nevada, USA, May 4-7, 2009, Basil R. Marple, Margaret M. Hyland, Yuk-Chiu Lau, Chang-Jiu Li, Rogerio S. Lima, and Ghislain Montavon, Ed., ASM International, Materials Park, OH, 2009.

Antoine Bacciochini, Ghislain Montavon, Alain Denoirjean, and **Pierre Fauchais**, Faculty of Sciences and Technologies, SPCTS, UMR CNRS 6638, University of Limoges, 123 Avenue Albert Thomas, 87060 Limoges Cedex, France; and **Jan Ilavsky**, Argonne National Laboratory, Advanced Photon Source, 9700 South Cass Avenue, Argonne, IL 60439. Contact e-mails: antoine.bacciochini@orange.fr and ghislain.montavon@unilim.fr.

nanometers to a few micrometers. SPS consists, besides other types of injection, of mechanically injecting within the plasma flow a suspension of sub-micrometer-sized or nanometer-sized particles through an injector of diameter of the order of 100 μm. Upon penetration within the plasma flow, the liquid stream encounters two mechanisms, fragmentation and vaporization (Ref 1). In a first approximation and whatever the suspension stream characteristic dimension (from a few micrometers to a few hundreds of micrometers in diameter), the fragmentation duration is at least two orders of magnitude shorter than the vaporization (Ref 2). Droplets encounter then liquid phase evaporation that leads to the formation of single particle or aggregates of a few particles, depending on the size of the suspension droplets and the particles. Then, these particles melt and form liquid drops that impact, spread and solidify to form flattened lamellae of equivalent diameters between a few hundred nanometers to a few micrometers and of average flattening ratio varying from 1 to 2 (Ref 7). The coatings, more or less cohesive, result from the stacking of such lamellae. Their architecture evolves from nearly fully dense to very porous, with a smooth (homogeneous) or irregular (heterogeneous) surface morphology, according to the operating parameters among which plasma power parameters (plasma torch operating mode, plasma flow mass enthalpy, spray distance, etc.), suspension properties (particle size distribution, powder mass percentage, viscosity, surface tension, etc.), and substrate characteristics (topology, temperature, etc.) play relevant roles.

Moreover, SPS coatings exhibit a typical ''granular'' structure, made of (Ref 8): (i) well molten particles (W) forming flattened lamellae; (ii) unmolten particles (U) that exhibit the shape of the initial feedstock (that depends upon its manufacturing process) corresponding to particles that have not traveled within the warm core of the plasma flow but rather in its colder fringes; (iii) small spherical grains corresponding to small molten particles (i.e., particles that have traveled within the warm plasma core) that have resolidified (R) prior to their impact upon the substrate. Tingaud et al. (Ref 8) demonstrated that the fraction of unmolten and resolidified particles was significantly influencing the coating architecture: the higher the $(U+R)/W$ fraction, the more porous the coating.

Nevertheless, architectures of SPS coatings, in particular their pore size distribution and their formation mechanisms, are not really well understood yet. One of the reasons comes from the scale size difference between APS and SPS feedstock powder used (in the order of 10^8 when considering particle volume) and, very likely, from different manufacturing mechanisms.

In fact, the typical anisotropic lamellar structure of APS coatings is not anymore duplicated at smaller size when considering SPS coatings. Indeed, the particle flattening ratio (defined by the $\xi = D/d$ ratio where D represents the lamella equivalent diameter and d the impinging particle initial diameter, Ref 7) in SPS is much smaller compared to APS coatings.

Therefore, the anisotropic (orthotropic) structure of coatings made of lamellae in APS evolves to a more compact structure made of the stacking of quasi-spherical particles. A simplified model would be to compare this architecture to compact spherical arrangement like face-centered cubic (fcc, compacity: 0.747) structure with tetrahedral and octahedral voids in the lattice corresponding to void between particles. Such a modeled structural arrangement can provide an estimation of some pore characteristic dimensions as a function of particle sizes.

This paper aims at presenting some of the characteristic features of these coatings, particularly the void size distribution measured by ultra-small-angle x-ray scattering (USAXS) and helium pycnometry, and at proposing mechanisms leading to their formation.

2. Experimental Setups

2.1 Substrates

Stainless steel (304 L) and low carbon (0.1 wt.%) steel button-type substrates of 25 mm diameter and 20 mm thickness were used as substrates. They were pre-polished using SiC papers and diamond-slurry finished until mirror finishing with average roughness in the order of 0.02 μm.

Indeed, mechanical anchoring is the assumed adhesion mechanism of these coatings. Mechanical anchoring requires the average substrate roughness to be of the same order than the average thicknesses of lamellae. In conventional APS, the average particle diameter of ceramic feedstock is in the order of 30 μm and the average thickness of the lamellae, assuming a flattening ratio of 3 to 4, is about 1 to 2 μm. Grit-blasting substrates permit to generate an average roughness of this order. In SPS, average particle diameter is much lower, down to 50 nm in the present case. Assuming flattening ratios of 1 to 2, average thicknesses of lamella is about 25 to 50 nm. Polishing substrates permits to generate such an average roughness.

2.2 Feedstock and Suspensions

The suspension was made of ethanol (99.5%) with 20 wt.% of yttria-partially stabilized zirconia (YSZ, 13 wt.%) from Unitec Ceramic (Stafford, UK) of particle size distribution (d_{10}-d_{90}) ranging from 30 to 290 nm with an average distribution diameter (d_{50}) of 50 nm (supplier data). An electrosteric dispersant developed at SPCTS (made of a mixture of phosphoric esters) was used to reach the optimum suspension dispersion corresponding to the lowest suspension viscosity (around 2 mPa · s with the considered suspension mass load, Ref 9).

After mixing the powder with solvent and dispersant, the suspension was sonicated for 20 min in order to disperse to the maximum possible extend the remaining agglomerates.

2.3 Plasma Spray Parameters

Mechanical injection used in this study consists in a pressurized container in which the suspension is stored and forced through an injector of $d_i = 150$ μm internal

Table 1 Optimized spray operating parameters

Type	Sulzer Metco F4MB	
Anode internal diameter at plasma torch exit, mm	6	
Plasma gas mixture	Ar-He	Ar-H_2
Plasma gas flow rate, L · min^{-1}	40-20	55-5
Arc current intensity, A	500	
Plasma flow average mass enthalpy, MJ · kg^{-1}	12	15
Spray velocity, m · s^{-1}	0.5-1.5	
Spray distance, mm	30-50	
Scanning step, mm per pass	10	

diameter. At the injector exit, a liquid jet of diameter of about 1.9 × d_i is formed (Ref 10). After a certain distance, Rayleigh-Taylor type instabilities develop and drops are generated by primary atomization (i.e., without any additional atomizing gas flow). The injector is fixed on the torch nozzle in such a way that the suspension liquid stream penetrates in the plasma jet flow prior to its fragmentation by secondary atomization (i.e., shear forces induced by the plasma flow to the suspension liquid stream). The pressure applied to the suspension container was about 0.5 MPa, leading to a liquid stream velocity of about 22 m · s^{-1} at the injector exit (Ref 11).

A F4-type plasma torch (Sulzer-Metco, Wohlen, Switzerland) equipped with a 6 mm internal diameter nozzle was used to process the suspension and manufacture thick coatings by superimposing passes. Indeed, thin coatings of 20 to 30 μm thick were manufactured in 30 passes (i.e., average deposited thickness per pass of about 0.8 to 1 μm). Prior to spraying, substrates were preheated to an average surface temperature of about 250 °C (measurement by infrared pyrometer in the 8-14 μm wavelength range). At the end of the spray cycle, average sample temperatures were in the order of 450 to 500 °C. Thicker coatings were also manufactured by superposition of 20 μm thick layers with cooling to room temperature and pre-heating to about 250 °C between each layer. Power and injection parameters were optimized in previous works (Ref 12, 13) and are displayed in Table 1.

2.4 Characterization Protocols

2.4.1 Scanning Electron Microscopy. Morphologic and microstructural characterizations were performed by scanning electron microscopy (SEM, Phillips XL30), either in the secondary electron (SE) or in the backscattered electron (BSE) modes. The SE mode permits higher resolutions compared to the BSE mode (in the order of 50 nm compared to about 150 nm), whereas the BSE mode can enhance contrast between phases, particularly between the YSZ matrix and the pores.

Analyses were performed on cross-sectioned and polished coatings (sectioning using a diamond saw in an oil medium, pre-polishing using grit-SiC papers of various downsizing grades and polishing using diamond suspensions of various particle diameter, from 9 down to 1 μm). Samples were coated with a sputtered conductive Au/Pt thin layer prior to analyses.

A Jeol JSM-7400F FESEM (field emission scanning electron microscope) was used for fractography facieses analyses. Indeed, FESEM permits higher resolutions compared to SEM due to its field emission gun (in the order of 2 nm in the present study); that is, one to two orders of magnitude higher than with SEM. For fractography facieses analyses, YSZ coatings were removed from the steel substrate by acid pickling of the substrate in an HCl and HNO_3 (50-50% in volume) mixture. The coatings were then manually cracked and coated with a conductive Au/Pt thin layer.

2.4.2 Pore Network Connectivity. Several techniques can be implemented to quantify the pore network connectivity to the substrate, particularly gas permeation and electrochemical impedance spectroscopy (EIS) where an electrolytic solution percolates through the connected pore network to react with the substrate (Ref 6). To assess solution percolation through the pore network, a simplified percolation test using water as wetting agent can be easily implemented to estimate the minimum pore size that can be discriminated. This test is justified by the Washburn equation as follows:

$$p \times d = -4\gamma \times \cos(\theta) \quad \text{(Eq 1)}$$

where p represents the surrounding pressure (Pa), d the pore diameter (m), γ the liquid surface energy (N · m^{-1}) and θ the contact angle between the coating material and pure water.

Other way to access to open pore fraction is employing gas adsorption phenomena, using helium pycnometry. Principle of gas adsorption allows measuring the true volume of sample. Indeed, gas atoms form a single layer on the total surface of material and penetrate into open and connected porosity. This technique has already been successfully employed to determine plasma coating density (Ref 14). The sizes of gas molecules offer a very high resolution, equivalent to helium atoms size (in the order of a few Angstroms). Nevertheless, this technique only considers open porosity and ignores single voids and closed porosity. An AccuPyc 1330 (Micromeritics, Norcross, GA, USA) was implemented to address open void content of SPS coatings.

2.4.3 X-Ray Microstructural Characterizations. High energetic photons beam allows measuring the coatings void content and size distribution by scattering of incident x-ray beam. USAXS measurements were conducted on beam line 32-ID at Advanced Photon Source (Argonne National Laboratory, Argonne, IL, USA) (Ref 15). At this beam line, a Bonse-Hart double crystal diffraction optics allows recording USAXS scattering curves (SC) using a photodiode detector with an angular resolution of 0.0001 $Å^{-1}$ at a q (scattering vector) range from 10^{-4} to 1 $Å^{-1}$ (Ref 16). The scattering vector q is a typically used quantity in small-angle scattering and relates to the diffraction angle (2θ), as known from x-ray diffraction, via the relationship (Eq 2):

$$q = 4\pi/\lambda \times \sin(\theta) \quad \text{(Eq 2)}$$

where λ is the x-ray wavelength (m). Combining this equation with Bragg's law, the length scale, L, probed at a

given q range follows the general inverse relationship (Ref 17) (Eq 3):

$$L \sim 2\pi/q \quad \text{(Eq 3)}$$

The USAXS device includes a double crystal monochromator for photon energy selection and two mirrors for harmonic rejection. This instrument delivers approximately 10^{13} photons per second in a 1 mm^2 area at the sample position, over the energy range, 16.9 keV, of incident photons 8-18 keV. The selected photon energy corresponds to a wavelength of 0.775 Å. The size of the x-ray beam is controlled by the incident beam slits, after which the first four-reflection crystal pair acts as the ''collimator''. The ion chamber measures the photon flux incident on the sample. The second four-reflection crystal pair acts as the ''analyzer''. The x-ray scattering from the sample is measured by rotating the analyzer and recording the scattered photons received by the detector. USAXS data are fully corrected for all instrument effects and analyzed using *Igor Pro** software from WaveMetrics Inc. (Oswego, OR, USA) coupled to *Irena** package (Ref 18), developed for analyzing small angle scattering data.

Phases present in the powder and coatings were determined by x-ray diffraction (XRD) using a Siemens D5000 diffractometer (θ-2θ) equipped with Soller's slit of 0.2 mm in front and 1 mm back. Cu-Kα x-ray radiation ($\lambda = 1.54056$ Å) was used. A Sol-X energy dispersive x-ray detector permitted to discard the substrate fluorescence. The angular range was 20-90°, the step size was 0.02° and the time per step was 1 s. The crystalline phases of zirconium oxide (i.e., monoclinic, tetragonal and cubic) were identified with JCPDS files 00-037-1484, 00-042-1164 and 00-027-0997, respectively. The 26-34° range corresponding to the $\{111\}_{c,m}$ reflections permits to discriminate the monoclinic phase from the cubic and tetragonal (c and t) ones. This specific range was investigated with a scan step of 0.01° and a time per step of 2 s.

3. Results and Discussion

3.1 Limitations of SPS Coating Architecture Analysis by SEM on Polished Cross-Sections

In the case of APS coatings, the void content quantification can be performed using stereological protocols coupled with image analysis carried out on BSE-SEM randomly captured pictures along the structure to be analyzed, among other possible protocols (Ref 6). This technique requires, of course, adequate polishing protocols to avoid, or at least limit to the maximum possible extend, polishing artifacts (i.e., scratches, pull-outs, etc.) occurring during the cutting and polishing steps. Moreover, the resolution of the pictures does not permit to discriminate the smallest features (i.e., smaller than the image resolution) of the pore network. This technique is nevertheless very widely used to analyze void content and crack network of APS coating since most of the feature sizes are usually higher than the SEM resolution.

However, the decrease in feedstock particle size encountered in SPS leads to much finer coating structures and accordingly to much smaller voids sizes. Two problems have to be solved in such a case, sample preparation by polishing and resolution limit of captured SEM pictures. Figure 1 displays the architecture of three SPS YSZ coatings manufactured with identical operating parameters

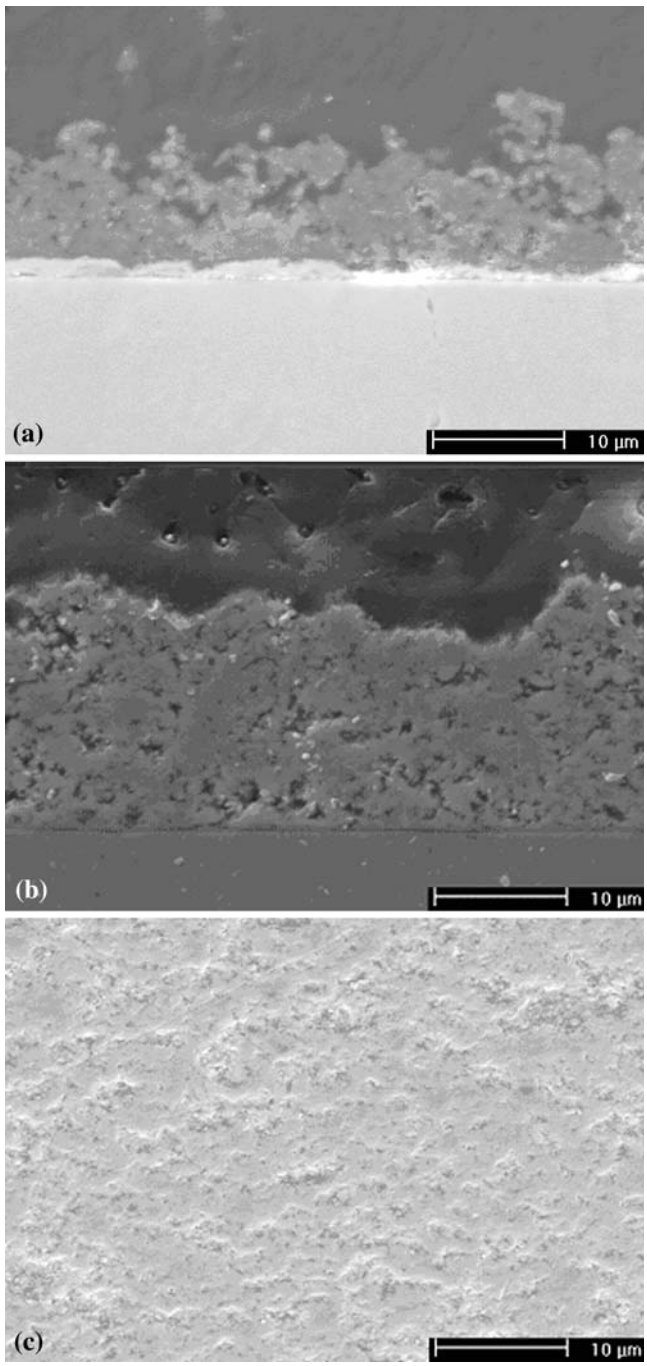

Fig. 1 Cross-sectional views of SPS YSZ coatings sprayed with identical operating parameters and polished with different protocols

*These software packages can be accessed at http://www.wavemetrics.com/ and http://usaxs.xor.aps.anl.gov/staff/ilavsky/irena.html.

(Table 1), but different thicknesses. Polishing protocols were ''optimized'' by three different development centers of polishing system vendors. Obviously, the architectures appear very different from each other (whereas it is assumed to be the same in the three displayed cases). Cutting and polishing protocols obviously induce artifacts and modify the apparent coating architecture. In fact, the smaller size of abrasive tool is about 1 μm (diamond suspension). Moreover, the resolution limit of SEM is not able to address voids and cracks of characteristic size smaller that the system resolution, in the order of 100 nm in the present case; that is, a resolution smaller that the average feedstock size ($d_{50} = 50$ nm).

One can hence conclude that quantification of void content from analyses carried out on coating cross-sections is not adequate for this type of structure.

Another way to observe the coating architecture without modification of its structure by polishing artifacts is fractography. As depicted in Fig. 2, the coating architecture is not made of flattened particles, but mostly formed by quasi-spherical grains stacked together. Contrary to APS coatings structure, vertical and horizontal cracks are not observed. Voids that can be typified in a first approximation as globular pores are visible in between these spheres.

3.2 Architecture of SPS Thick Coating

3.2.1 FESEM Fractography. This type of sample preparation appears as a protocol permitting to assess the coating structure without any induced artifacts due to the polishing step. Figure 3 display two typical features in a SPS coating architecture: a through-thickness granular one and a layered one that develops at the coating/substrate interface.

Besides the granular structure, some columnar stacking defects developing from the coating/substrate interface to the upper part of the coating are visible (Fig. 4). Those stacking defects emerge at the coating top surface (Fig. 5). Their density, function of the operating parameters, is estimated to be of the order of 3-4 cracks per millimeter.

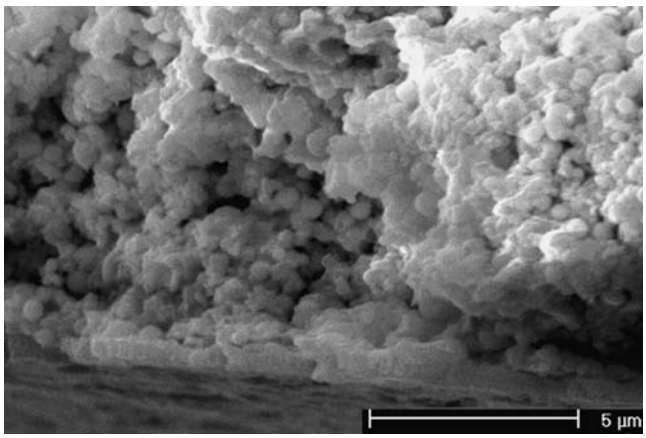

Fig. 2 SEM fractography of SPS YSZ coating

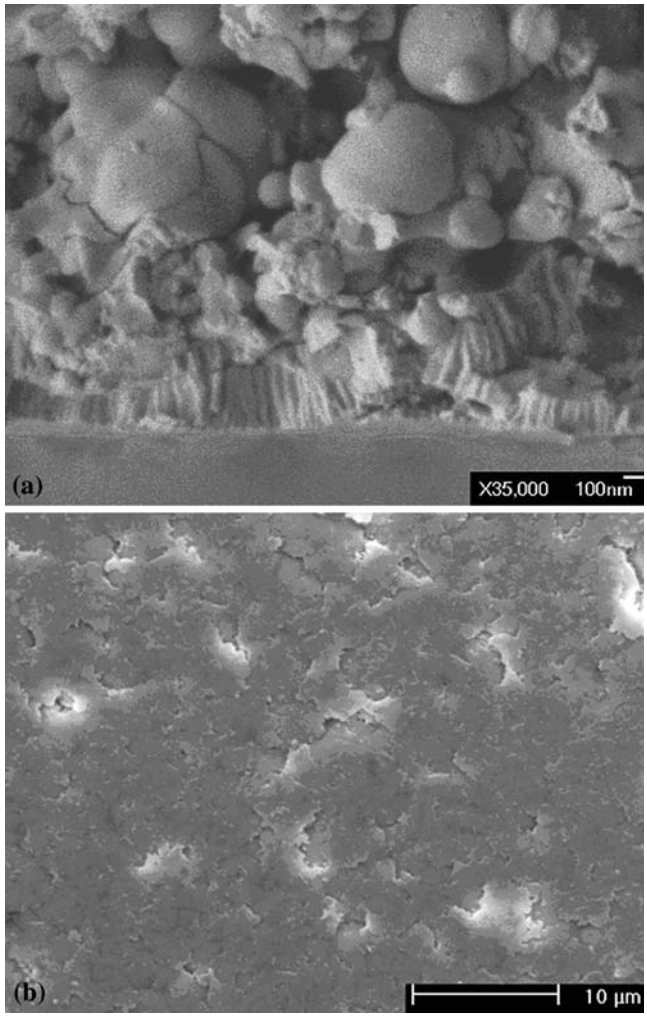

Fig. 3 (a) FESEM fractography of YSZ thick coating. (b) Structure of the coating layer at the substrate/coating interface

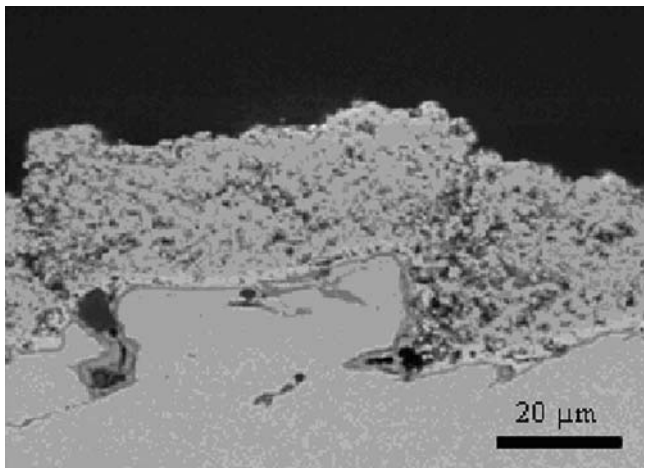

Fig. 4 Columnar stacking defects developing through the thickness of a SPS coating manufactured on a rough substrate (average roughness, R_a, in the order of 2 μm)

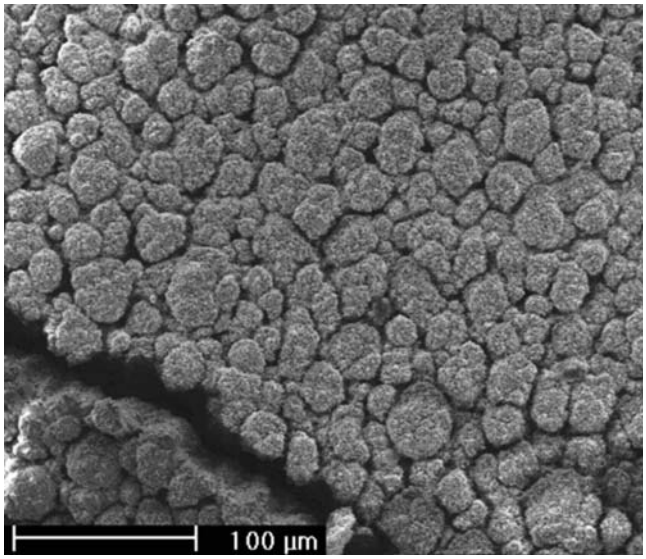

Fig. 5 Top view of a free-standing SPS coating surface

Very likely, those columnar defects develop due to the shadow effect induced by the substrate surface topology: as soon as a stacking defect is formed, it is not filled up by following impinging particles and hence continues to growth and develop through the thickness during coating manufacturing. The formation of such stacking columnar defects is very dependent on the substrate surface roughness: the higher the roughness, the higher these stacking defects (Fig. 4).

At the substrate/coating interface, a fairly dense lamellar layer of average thickness thinner than 1 µm develops (Fig. 3a). This thin and fairly dense layer is formed by the stacking of flattened particles exhibiting flattening ratios much higher than in the rest of the coating. Indeed, one can assume that once a thin layer of YSZ is formed, the thermal resistance would significantly increase, hence delaying the cooling of subsequent impinging particles. This would allow the flattened particles to remain in a molten state for longer times. Since particles are nanometer-sized, the surface tension at the end of the flattening stage plays a more important effect compared to the one on micrometer-sized flattened particles. Complete recoil of molten lamellae leads to the formation of spherical particles and ultimately to the granular structure.

Closer observations of the substrate/coating interfaces show that the columnar stacking defects originate mostly from stacking defects in the lamellar layer. Figure 3(b) identifies areas where interfacial voids or resolidified particles are detectable. Those stacking defects correspond very likely to the connection point of open pores between the substrate and the surface of the coating.

Besides, the density of stacking defects in the lamellar layer depends upon operating parameters. Figure 6 depicts the interfaces of coatings manufactured with two plasma forming gas mixtures, Ar-H_2 (Fig. 6a) and Ar-He (Fig. 6b). Operating the plasma torch under an Ar-H_2 plasma gas mixture favors the restrike operating mode (Ref 7) characterized by large relative voltage variations (i.e., $\Delta V/V \sim 1.0$) and leads to a less homogeneous processing of suspensions compared to an Ar-He plasma gas mixture that favors the take over operating mode (i.e., $\Delta V/V \sim 0.3$). As a consequence, more stacking defects are visible in the lamellar layer processed with an Ar-H_2 plasma gas mixture.

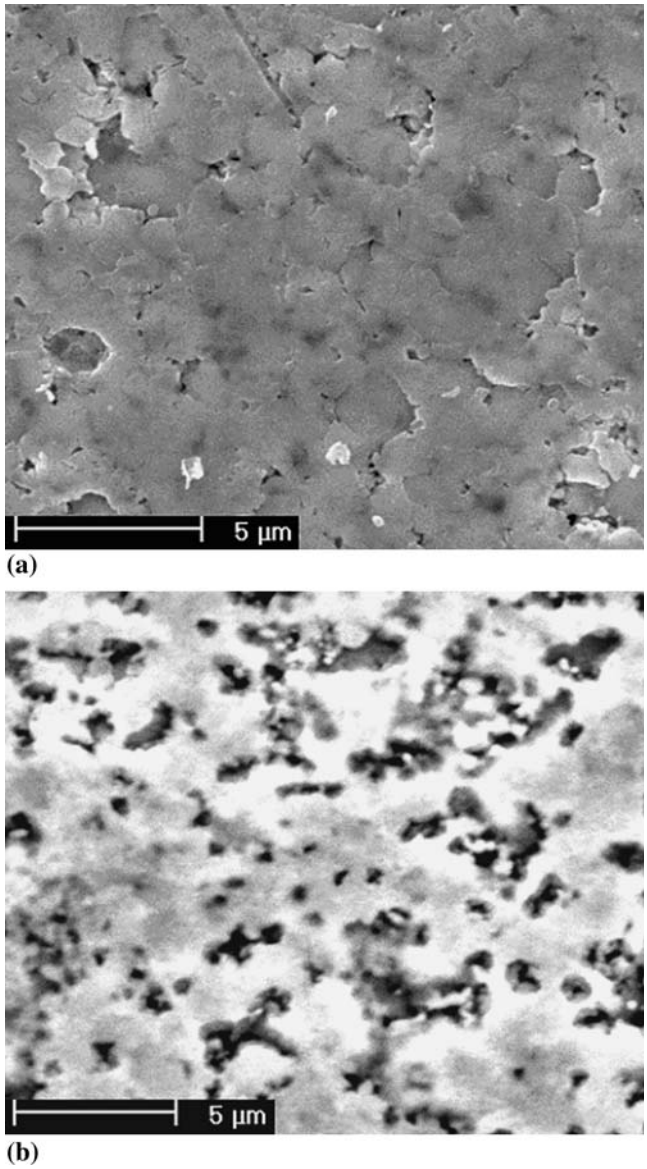

Fig. 6 Comparison of substrate/coating interfaces in function of plasma gas mixture. (a) Ar-He gas mixture and (b) Ar-H_2 gas mixture (SE-SEM pictures)

Besides the more homogeneous lamellar layer structure provided by the suspension processing with an Ar-He plasma gas mixture, the flattening ratio of lamellae seems lower than the one of particles processed with an Ar-H_2 gas mixture. Indeed, the Ar-H_2 plasma gas mixture leads to a very large distribution in particle flattening ratios. Between those lamellae, angular particles, corresponding

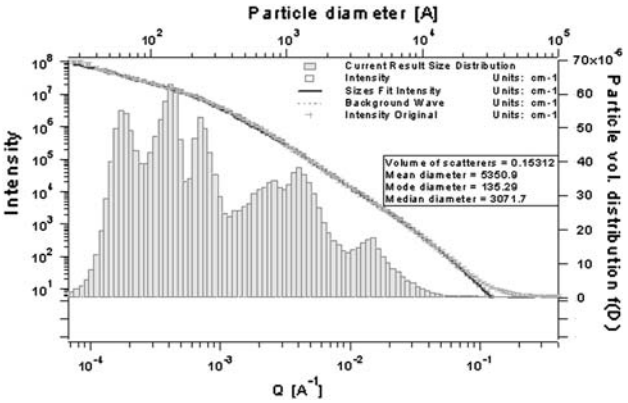

Fig. 7 Scattering curve of YSZ coating with void distribution

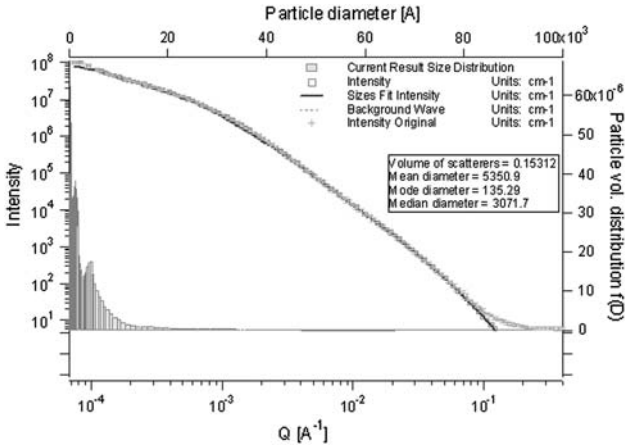

Fig. 8 Voids volume representation on scattering curve

Table 2 USAXS total void content measurements

	Plasma gas mixture			
	Ar-He		$Ar-H_2$	
Spray distance, mm	30	50	30	50
Volume of scatters, %	14.3	18.4	12.9	19.3
Mean diameter, nm	538	630	596	567
Mode diameter, nm	5.5	5.4	5.5	7.1

to untreated ones (particle are manufactured by the fused and crushed process), are detectable.

3.2.2 Ultra-Small-Angle X-Ray Scattering Measurements. Data extraction using Irena software allowed accessing to the void size distribution, including void mean and median diameters. Mode diameter, which represents void diameter range that includes the highest number of voids, is another data depicting pore size distribution.

A typical fitted and analyzed curve by Irena software is shown in Fig. 7. Volume of scattering corresponds to the total void content. Table 2 displays the USAXS measurements as a function of some considered operating parameters. The total pore content varies from 14.3 to 19.3% and the mean diameter is between 500 and 630 nm.

The results on porosity rate confirm that operating parameters tailored the coating architecture and voids structure. Indeed, USAXS measurements indicate that in case of Ar-He and $Ar-H_2$ plasma gas mixtures the total void content remains approximately the same. Considering two spray distances, 30 and 50 mm, another tendency could be pointed out: a shorter spray distance of 30 mm permits to manufacture a denser coating than a longer spray distance of 50 mm, thanks to a higher particle momentum upon impact and very likely a higher particle temperature.

These analyses using transmitted high energetic photons beam proved that average diameters of voids are nanometer and sub-micrometer-sized. This fact defends the previous established limitations of stereological processes combined to SEM polished cross-sectional observations. Moreover, a large number of voids displays average diameter values from 5.5 to 7.5 nm (i.e., mode diameter values which represent size classes of voids). Figure 8 depicts a typical scattering curve with normal axis to appreciate the volume of voids as a function of their size: the nanometer-sized pores represent the highest population of voids in SPS coatings.

Furthermore, the scattering curves exhibit multimodal distribution of void diameters. Each mode diameter can be estimated and four void size classes can be discriminated in a first approximation: [1-10 nm[, [10-20 nm[, [20-43 nm[, and [43-100 n[.

3.2.3 Pore Network Connectivity. The connectivity of a pore network is related to the quantity of voids which connects the substrate to the surrounding atmosphere. The simplistic test of de-ionized water droplet percolation through the coating permits to determine the smallest open pore diameter into which the water is able to percolate, merely using Washburn's equation (Ref 1). Contact angle, θ, between zirconia and de-ionized water was measured to be about 59°, the surface energy, γ, of de-ionized water is 72.8 $mN \cdot m^{-1}$. At atmospheric pressure (about 10^5 Pa), pure water percolates into open voids of equivalent diameter equal or larger than 1.5 μm.

The calculation of connectivity diameter proves that the classical coating connectivity measurement by EIS cannot be representative of the connected pore network since the electrolytic solution is diluted and has a surface energy of the same order than that of de-ionized water. So the ionic solution cannot percolate through the entire connected network. EIS analysis does hence not seem to be a reliable protocol to quantify the connectivity of SPS coatings.

Nevertheless, gas adsorption analyses reveal SPS coatings closed void contents from 1.9 to 4.1% depending upon the operating parameters, Table 3. For micrometer-sized ceramic coatings manufactured by APS, relative connected void contents are very frequently measured around 80%. Very likely, 9 to 15% of open voids results from columnar stacking defects (cf. Fig. 5), which develop

Table 3 Open porosity measurements by helium gas adsorption

	Plasma gas mixture			
	Ar-He		$Ar-H_2$	
Spray distance, mm	30	50	30	50
Non-connected void content, %	1.9	3.5	3.3	4.1
Estimated open void content, %	12.4	14.9	9.6	15.2
Relative connected void content, %	86.7	81.0	74.4	78.8

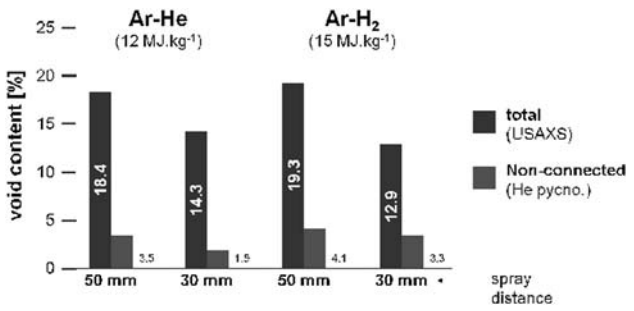

Fig. 9 Porous architecture quantification vs. operating parameters

from surface anfractuosities due to a shadow effect (Ref 8). Figure 9 depicts the discrimination of voids for two plasma gas mixtures at spray distances of 30 and 50 mm. At first, an Ar-He plasma gas mixture leads to a lower closed void content compared to an $Ar-H_2$ mixture. This is very likely induced by lower particle momentum upon impact together with higher particle viscosity (due to lower particle temperature). At second, a decrease in spray distance leads to a decrease in the total void content. These results demonstrate a synergy between plasma gas mixtures, plasma enthalpy and plasma torch operating mode in tailoring SPS coating void architecture. Considering for example thermal barrier coatings as application, using an $Ar-H_2$ plasma gas mixture with 30 mm spray distance would permit to increase the total void content with the lowest connected void fraction.

3.2.4 Modeling Voids in SPS Structure. The correlation between pore sizes as measured by USAXS and architecture observed from FESEM fractographies incite to propose a trivial model for nanometer-sized voids presents in SPS coating. Such architecture can be depicted in a simplistic way by a compact stacking of spherical particle, like face-centered cubic (fcc) in a Bravais's network.

In such cases, the octagonal and tetragonal spaces could be assimilated to average void diameters. The characteristic size of the tetrahedral voids of the fcc system is equal to $D_t = 0.225 \times d$ (where d represents the diameter of the particles and D_t the diameter of the tetrahedral space). Identically, the octahedral void characteristic size is equal to $D_o = 0.414 \times d$. Table 4 displays the characteristic size values of spaces in the equivalent lattices for different values of feedstock particle diameter.

Table 4 Void characteristic dimensions using tetrahedral and octahedral spaces models

Feedstock particle diameter range	Value, nm	Tetrahedral space characteristic size D_t, nm	Octahedral space characteristic size D_o, nm
d_{10}	30	7	12
d_{50}	50	11	21
d_{90}	290	65	120

Of course, such an approach does not consider particle flattening or the stacking of particles of various sizes. It nevertheless defines orders of magnitude for average pore sizes. Moreover, the calculated void sizes compared to the measured size distribution modes show a good correlation. As shown in Table 4, the estimated pore sizes are 4 times smaller than the BSE-SEM resolution and are approximately of the same order of magnitude than the SE-SEM resolution. These comparisons demonstrate one more time that observations from polished cross-sections with classical SEM are not adequate to quantify SPS coating void contents.

3.2.5 Phase Identification. X-ray diffraction analyses were performed on powder feedstock and samples manufactured with an Ar-He plasma gas mixture at two different spray distances: 30 and 50 mm. The XRD patterns permit to index the zirconia phases present in the coatings. A solid solution of the cubic and tetragonal zirconia is predominant in the coating. A peak of low intensity of monoclinic phase $\{111\}_m$ appears at $2\theta = 28.86°$. Monoclinic phase develops very likely during coating manufacturing since the average manufacturing temperature is fairly high (500 °C) and the local transient temperature even higher (very likely, up to 1000 °C).

However, a more precise analysis carried out on this small angular range (26-34°) has not permitted to quantify the fraction of monoclinic phase. One can hence conclude that its relative fraction is less than a few percents. Consequently, one could assume that the volume variation associated to this martensitic transformation would not play a relevant role in developing voids or cracks in the coating structure.

4. Concluding Remarks

Thick coatings manufactured by SPS process exhibit a specific architecture made of a granular structure through the coating thickness and a lamellar layer at the substrate/coating interface.

Due to polishing artifacts, stereological protocols based on image analysis do not seem appropriate anymore to quantify pore network architecture of the considered SPS YSZ coatings manufactured from particles of average size of about 50 nm. Moreover, observations tend to indicate that average void diameter is one to two orders of magnitude smaller than the resolution limit of conventional SEM systems. Besides, one can easily demonstrate also that EIS protocol is not adequate to quantify the pore

network connectivity since most of the aqueous solutions would not percolate through connected pores of characteristic size smaller than about 1.5 μm. Nevertheless, FESEM fractography observations permit to discriminate pores and estimate their characteristic dimensions and hence to better understand the coating manufacturing mechanism. Moreover, a simplistic model based on Bravais' networks correlates with pore sizes measurements by USAXS measurements and could estimate the smallest sizes of nanometer-sized voids.

Ultra small angle x-ray scattering analyses allow the quantification of coating pore content and combined with gas adsorption measurements, the discrimination of connected pores and closed voids. Such combined analyses point out the differences in coating architecture depending upon operating parameters. In particular, this study proves that the plasma gas mixture has a major impact on coating architecture and that the spray distance affects the pore content in a more emphasized way than in APS.

Acknowledgments

Use of the Advanced Photon Source at Argonne National Laboratory was supported by the U. S. Department of Energy, Office of Science, Office of Basic Energy Sciences, under Contract No. DE-AC02- 06CH11357.

References

1. E. Brousse, G. Montavon, P. Fauchais, A. Denoirjean, V. Rat, J.-F. Coudert, and H. Ageorges, Thin and Dense Yttria-Partially Stabilized Zirconia Electrolytes for IT-SOFC Manufactured by Suspension Plasma Spraying, *Thermal Spray Crossing Borders*, E. Lugscheider, Ed., June 2-4, 2008 (Maastricht, The Netherlands), DVS, Düsseldorf, Germany, 2008, p 547-552
2. P. Fauchais, Understanding Plasma Spraying, *J. Phys. D: Appl. Phys.*, 2004, **37**, p R86-R108
3. K. Wittman, F. Blein, J. Fazilleau, J.-F. Coudert, and P. Fauchais, A New Process to Deposit Thin Coatings by Injecting Nanoparticles Suspension in a DC Plasma Jet, *Tagungsband Conference Proceedings*, E. Lugscheider, Ed., DVS, Düsseldorf, Germany, 2002, p 519-522
4. P. Padture, K. Schlichting, T. Bhatia, A. Ozturk, B. Cetengen, E. Jordan, M. Gell, S. Jiang, P. Strutt, E. Garcia, P. Miranzo, and M. Osendi, Towards Durable Thermal Barrier Coatings with Novel Microstructures Deposited by Solution-Precursor Plasma Spray, *Acta Mater.*, 2001, **49**, p 2251-2257
5. L. Pawlowski and P. Fauchais, Thermal Transport Properties of Thermally Sprayed Coatings, *Int. Mater. Rev.*, 1992, **36**, p 271-289
6. G. Antou, G. Montavon, F. Hlawka, A. Cornet, C. Coddet, and F. Machi, Evaluation of Modifications Induced on Pore Network and Structure of Partially Stabilized Zirconia Manufactured by Hybrid Plasma Spray Process, *Surf. Coat. Technol.*, 2004, **180-181**, p 627-632
7. L. Bianchi, ''D.C. and R.F. Plasma Spraying of Ceramic Coatings: Mechanism of the Formation of the First Layer and Its Link with Coatings Properties,'' Ph.D. Thesis, University of Limoges, France, 1995 (in French)
8. O. Tingaud, A. Grimaud, A. Denoirjean, G. Montavon, V. Rat, J.-F. Coudert, P. Fauchais, and T. Chartier, Suspension Plasma-Sprayed Alumina Coating Structures: Operating Parameters vs. Coating Architecture, *Thermal Spray Crossing Borders*, E. Lugscheider, Ed., June 2-4, 2008 (Maastricht, The Netherlands), DVS, Düsseldorf, Germany, 2008, p 323-328
9. J. Fazilleau, ''Contribution to the Understanding of Phenomena Involved in Finely Structured Oxide Coatings Manufactured by Suspension Plasma Spraying,'' Ph.D. Thesis, University of Limoges, France, 2003 (in French)
10. C. Delbos, ''Contribution to the Understanding of Ceramic (YSZ, Perovskite, etc.) or Metallic (Ni, etc.) Particles Injection by a Liquid Carrier in a Plasma Jet to Manufacture Finely-Structured Coatings for SOFC,'' Ph.D. Thesis, University of Limoges, France, 2004 (in French)
11. K. Wittmann, F. Blein, J.-F. Coudert, and P. Fauchais, Control of the Injection of an Alumina Suspension Containing Nanograins in a d.c. Plasma, *Thermal Spray 2001 : New Surfaces for a New Millenium*, C.C. Berndt, K.A. Kohr, and E. Lugscheider, Ed., ASM International, Materials Park, OH, 2001, p 519-522
12. C. Monterrubio-Badillo, H. Ageorges, T. Chartier, J.-F. Coudert, and P. Fauchais, Preparation of $LaMnO_3$ Perovskite Thin Films by Suspension Plasma Spraying for SOFC Cathodes, *Surf. Coat. Technol.*, 2006, **12-13**, p 3742-3756
13. P. Fauchais, V. Rat, J.-F. Coudert, T. Chartier, and L. Bianchi, Understanding of Suspension d.c. Plasma Spraying Finely Structured Coatings for SOFC, *Plasma Sci. IEE Trans.*, 2005, **2**, p 920-930
14. J.A. Curran and T.W. Clyne, Porosity in Plasma Electrolytic Oxide Coatings, *Acta Mater.*, 2006, **54**(7), p 1985-1993
15. J. Ilavsky, P.R. Jemian, A.J. Allen, F. Zhang, L.E. Levine, and G.G. Long, Ultra-Small-Angle X-Ray Scattering at the Advanced Photon Source, *J. Appl. Crystallogr.*, 2009, **42**, p 347-353
16. O. Glatter and O. Kratky, *Small Angle X-Ray Scattering*, Academic Press Inc., New York, 1982, p 54-81
17. T. Narayanan, Synchrotron Small-Angle X-Ray Scattering, *Soft Matter Charact.*, 2008, **36**, p 899-948
18. J. Ilavsky and P.R. Jemian, Irena: Tool Suite for Modeling and Analysis of Small-Angle Scattering, *J. Appl. Crystallogr.*, 2009, **42**, p 347-353